HHS Public Access

Author manuscript

Comput Biol Med. Author manuscript; available in PMC 2017 October 01.

Published in final edited form as:

Comput Biol Med. 2016 October 1; 77: 173–181. doi:10.1016/j.compbiomed.2016.07.013.

Automatic Deformable Surface Registration for Medical Applications by Radial Basis Function-Based Robust Point-Matching

Youngjun Kim[1,2], **Yong Hum Na**[2], **Lei Xing**[2], **Rena Lee**[3], and **Sehyung Park**[1,*]

[1]Center for Bionics, Korea Institute of Science and Technology, Seoul, South Korea

[2]Department of Radiation Oncology, Stanford University School of Medicine, Stanford, CA, United States

[3]Department of Radiation Oncology, Ewha Woman's University College of Medicine, Seoul, South Korea

Abstract

Deformable surface mesh registration is a useful technique for various medical applications, such as intra-operative treatment guidance and intra- or inter-patient study. In this paper, we propose an automatic deformable mesh registration technique. The proposed method iteratively deforms a source mesh to a target mesh without manual feature extraction. Each iteration of the registration consists of two steps, automatic correspondence finding using robust point-matching (RPM) and local deformation using a radial basis function (RBF). The proposed RBF-based RPM algorithm solves the interlocking problems of correspondence and deformation using a deterministic annealing framework with fuzzy correspondence and RBF interpolation. Simulation tests showed promising results, with the average deviations decreasing by factors of 21.2 and 11.9, respectively. In the human model test, the average deviation decreased from 1.72 ± 1.88 mm to 0.57 ± 0.66 mm. We demonstrate the effectiveness of the proposed method by presenting some medical applications.

Keywords

Mesh deformation; Deformable registration; Automatic correspondence; Radial basis function; Robust point matching

*Corresponding author: Sehyung Park, Ph.D. Principal Researcher, Center for Bionics, Biomedical Research Institute, Korea Institute of Science and Technology. Address: Hwarangno 14-gil 5, Seongbuk-gu, Seoul 136-791, South Korea, Tel.: +82 2 958 5643. junekim@kist.re.kr, yonghum@gmail.com, lei@stanford.edu, renalee@ewha.ac.kr, sehyung@kist.re.kr

Conflict of Interest Statement

We (Youngjun Kim, Yong Hum Na, Lei Xing, Rena Lee, and Sehyung Park) declare that we have no proprietary, professional or other personal interest of any nature or kind in any product, service and/or company that could be construed as influencing the position presented in, or the review of, the manuscript entitled, "Automatic Deformable Surface Registration and the Medical Applications by Radial Basis Function based Robust Point-Matching".

1. Introduction

1.1 Background

Image registration has been an essential technique in medical applications including multi-modality image registration for diagnosis or planning, statistical analysis for population study, in-room surgery/treatment guidance, and intra- or inter-patient study [1, 2]. With the extensive use of multi-modal imaging and new treatment techniques, the requirement for a robust registration algorithm for comparing or fusing images representing the same structures obtained under different conditions or modalities is ever increasing. Medical image registration has long been classified as rigid or affine; however, deformable transformation is now available as an alternative method for improving registration accuracy. Deformable (or non-rigid) registration is comparatively more complicated and involves modeling the local distortion in addition to translation, rotation, and scaling. According to the type of data, deformable registration is categorized into volumetric or surface. Volumetric registration uses the voxel information of volume images. Many approaches have been actively investigated, including mutual information (MI) [3], free-form deformation (FFD) based on B-spline [4, 5], and Demon deformable registration [6, 7]. Deformable surface registration (DSR) registers two surface meshes consisting of point and triangular elements. Non-rigid point registration is a well-known method in this category for registering two point sets [8, 9]. Many DSR approaches have been proposed robust high-speed automatic DSR has been difficult to achieve. Typically, the user must define the corresponding point sets manually; this is a tedious and time-consuming task, because it requires exploring and defining the fiducial points in 3D repeatedly. Automatic methods have been unstable or slow, with runtimes of tens of minutes for thousands of input points.

To overcome these difficulties, we propose a robust and fast technique for automatic DSR. The proposed method automatically determines the corresponding points and local transformations in a deterministic annealing framework. Every registration iteration consists of two steps, automatic correspondence finding and local deformation. Unlike previous methods, we use radial basis function (RBF) interpolation [10] for local deformation, which yields fast and stable solutions. We evaluate the accuracy and performance of the proposed method using synthetic simulation tests. The sample applications presented in this paper demonstrate the robustness and versatility of the proposed method, which enable its use in other medical fields such as patient setup for surgery or radiotherapy (RT) using 3D optical scanning, modification of radiotherapy planning, and patient-specific modeling.

1.2 Related Work

Various algorithms exist for non-rigid point set registration. In this section, we present an overview of the non-rigid registration methods and identify our motivation. Li et al. presented a template-based deformable registration by large-scale and fine-scale process [11]; however, their method requires a template model focusing only on single-view systems. Bonarrigo et al. proposed a non-rigid registration of partially overlapping surfaces from a deforming model by nonlinear physics-inspired deformation, with a computation time of 10 min for 9,600 points [12]. Recently, Myronenko and Song proposed a probabilistic method, Coherent Point Drift (CPD), for both rigid and non-rigid point set

registration [13]. They demonstrated promising results. However, naive CPD is rather slow, and it is not obvious that their fast implementation of non-rigid CPD outperforms the other methods. CPD originated from a registration method using Gaussian mixture models [14].

Robust point-matching (RPM) accepts two point sets as input and iteratively calculates the correspondence between the sets and transformation that registers them. Rather than assigning a one-to-one mapping for every pair of points, the correspondence is obtained in RPM using soft assignment in fuzzy logic [15]. Chui and Rangarajan developed thin-plate spline-based RPM (TPS-RPM) for non-rigid mapping, which yielded better results than rigid deformation did [16]. Xia et al. investigated an automatic non-rigid registration for whole body CT mice images [8]. Their method used skeletons for correspondence through RPM, and an intensity-based algorithm refined the transformation with spatial adaptation of the transformation's stiffness and RBF interpolation. However, the method involves volumetric registration, and they reported an average running time of 171 min for mice skeleton studies. Wang and Fei [9] proposed non-rigid B-spline-based point-matching (BPM), which combines B-spline-based local deformation with an RPM framework. They argued that compared to TPS-RPM, BPM could decrease the degrees-of-freedom from thousands of parameters to a small number of B-spline coefficients. However, despite demonstrating acceptable results, BPM remains computationally slow, with a reported average computing time of 45 min for input surfaces with 4,500 points. Other approaches to B-spline-based free-form deformation for volumetric registration include using Xie and Farin's hierarchical B-Splines [17], and more can be found in [4]. For robust and efficient surface deformation, RBF interpolation [10] can also be used. Its scale-independent characterization is well suited for reconstructing surfaces from non-uniformly sampled data. This analogy is perfectly applicable to our problem of local deformation from corresponding points of two input surfaces. We thus propose an RBF-based RPM to utilize these advantages to their fullest for yielding an efficient automatic DSR algorithm.

2. METHODS

2.1 Deformable registration framework

Given two point sets of a source surface S:{s_i, i = 1, 2, …, n_s} and a target surface T:{t_j, j = 1, 2, …, n_t}, the deformable registration problem is to determine an optimal spatial transformation f that deforms S to fit T. In general, s_i and t_j represent the spatial coordinates of the surface points in 3D, and f(s_i) is the coordinates of S that result from the deformable registration while preserving the topology. First, rigid transformation for global transformation f_{global} is calculated to provide suitable initial conditions for the local transformation f_{local}. To obtain f_{global}, we use point-to-plane iterative closest points (ICP) [18, 19], a widely used rigid transformation method. If the initial postures of S and T are considerably different, three pairs of corresponding points are required by the user input before applying ICP. ICP solves the optimization problem that minimizes the following error function.

$$E=\sum\left[\left(Rs_i+q-s_i'\right)\cdot n_i\right]^2 \quad (1)$$

where s_i, s_i', R, q, and n_i are the source points, s_i's projected points onto T with the direction of n_i, rotation matrix, translation vector, and s_i's normal vector, respectively.

After f_{global} roughly aligns S to T, a local transformation f_{local} is computed to change the local shape to minimize the deviations between $f_{global}(S)$ and T. For robust and fast computation of f_{local}, we propose an RBF-based RPM, with each iteration consisting of two steps: automatic correspondence finding and RBF deformation. The framework solves the interlocking optimization problems of the correspondence and the local transformation under the deterministic annealing scheme. Fig. 1 shows the deformable registration framework algorithm. In the deterministic annealing procedure, the algorithm searches for correspondences with a wide range in the beginning stages, while covering only the local range at the end. The parameter κ specifies the deterministic annealing temperature, which we determined to be reduced linearly by $\kappa_{n+1} = 0.90\,\kappa_n$. The temperature parameter κ weights the fuzziness regarding the distance in the cost function. We set the initial value of κ as $\kappa_0 = 0.5$, as suggested by Chui and Rangarajan [16], although κ_0 values did not significantly affect the results in the experiments. When the deformation results converge at a specified level (if the deviation change is below a threshold between successive iterations), we terminate the annealing procedure.

2.2 Automatic correspondence finding

Automatic correspondence finding has been a popular topic in character recognition and pattern matching [15]. A key RPM characteristic is that the correspondence is obtained by soft-assignment, rather than one-to-one mapping [8, 9, 15]. A point s_i of S relates to the points of T with a fuzzy ratio m_{ij},

$$m_{ij} = \frac{1}{\kappa} e^{\frac{\|t_j - f(s_i)\|^2}{2\kappa}} \quad (2)$$

for i = 1, 2, …, n_s, and j = 1, 2,…, n_t. The correspondence of S and T is obtained using a fuzzy matrix $M=\{m_{ij}\}$. M is more fuzzy at the beginning with larger κ, and the fuzziness decreases with smaller κ at the end of the deterministic annealing process. To reject the outliners, we define a point as a outlier if the point's distance to any point in the other surface is larger than $3\sqrt{\kappa}$ in the extra row and column ($i=n_s+1$, $j=n_t+1$) of M [9, 15]. The target point $\overline{t_i}$ on T corresponding to a source point s_i on S is computed as follows.

$$\overline{t_i} = \sum_{j=1}^{n_i} m_{ij} t_j \Big/ \sum_{j=1}^{n_i} m_{ij} \quad (3)$$

Fig. 2 and Fig. 5 show the correspondence finding (S: red, T: blue), with the computed corresponding points $\overline{t_i}$ displayed in black points.

2.3 RBF transformation for local deformation

Once the correspondence is determined, local transformation f_{local} is calculated using RBF. RBF is a powerful interpolation technique in multidimensional space, and mesh deformation is one of the best applications of RBF [10, 20]. The basis function $\varphi(r)$ is a real-valued function whose value depends on the distance from the feature points, hence the term radial. RBF constructs the interpolants as a linear combination of the basis functions as follows.

$$f_{local}(x) = p(x) + \sum_{i=1}^{n_s} w_i \cdot \phi(\| x - \overline{t_i} \|) \quad (4)$$

where p(x) is a linear polynomial of low degree, and the w_i are the real number coefficients of basis functions. We tested popular choices for the basis function $\varphi(r)$, such as the thin plate spline, multiquadric, and Gaussian funhctions, and we selected the multiquadric function $\varphi(r) = (r^2 + d^2)^{1/2}$ with a constant d. We empirically determined $\varphi(r)$ and d by testing the candidate basis functions and variables with sample patient data shown in Figs. 3, 5 and 8. In the specific case of the biharmonic spline in 3D, we can assume $p(x) = c_1 + c_2x + c_3y + c_4z$, with Eq.(4) written in matrix form as

$$\begin{pmatrix} A & P \\ P^{\mathrm{T}} & 0 \end{pmatrix} \begin{pmatrix} w \\ c \end{pmatrix} = B \begin{pmatrix} w \\ c \end{pmatrix} = \begin{pmatrix} f \\ 0 \end{pmatrix} \quad (5)$$

where $A_{ij} = \varphi(r)$ for i,j=1,…,n_s,

$$P = \begin{pmatrix} 1 & x_1 & y_1 & z_1 \\ 1 & x_2 & y_2 & z_2 \\ 1 & x_3 & y_3 & z_3 \\ 1 & x_4 & y_4 & z_4 \end{pmatrix}$$

$w = (w_1, w_2, \ldots, w_{ns})^T$, and $c = (c_1, c_2, c_3, c_4)^T$.

We obtain the coefficients of the basis functions w_i using the condition that s_i equals $\overline{t_i}$ for registration.

$$\overline{t_i} = f(s_i) = \sum_{i=1}^{Ns} w_i \cdot \phi(\| s_i - \overline{t_i} \|) \quad (6)$$

We can solve Eq.(6), because we have n_s pairs of s_i and t_i. We use singular value decomposition (SVD) to compute w and c.

$$\begin{bmatrix} w_1 & w_2 \cdots w_n & c_1 & c_2 & c_3 & c_4 \end{bmatrix}^{\mathrm{T}} = \mathrm{H}^{-1} \begin{bmatrix} \overline{t_1} & \overline{t_2} & \cdots \overline{t_n} & 0 & 0 & 0 & 0 \end{bmatrix}^{\mathrm{T}} \quad (7)$$

where H is a matrix that consists of RBF values.

With the calculated w and c from Eq.(7), we apply the RBF transformation for all the points of S using Eq.(4), and finally obtain the morphed source surface S'. For robust RBF transformation with dense points, we sample the corresponding points, instead of using the entire s_i point set, because SVD becomes unstable for matrix sizes larger than several thousand in our cases [10]. At each iteration, we down-sampled the source points s_i and computed the representative $\widetilde{s_i}$ by mesh decimation with randomized ratios, using $\widetilde{s_i}$ for correspondence finding and RBF deformation. This enables numerically stable computations for large n_s and n_t. We used SVD implemented by Numerical Recipes [21]. Fig. 3 illustrates an example of RBF-based RPM, which shows that S in red is deforming to register to T in blue through iteration.

2.4 Evaluation of RBF-based RPM

We performed simulation tests with synthetic data to estimate the accuracy of the proposed RBF-based RPM in an ideal situation. To evaluate the proposed method, we performed simulation experiments using a spherical model and a human head. First, we created a synthetic target surface by intentionally deforming a 10.0 mm diameter sphere with 772 points. To obtain the synthetic target surface for T, the spherical model was scaled by 20%, −10%, 15% in the x, y, z directions, respectively, and distorted using free-form deformation (FFD) with 4 * 4 * 4 nodes by moving the nodes in arbitrary directions. The original sphere for S was then registered to T using the proposed method, and the deviation was checked. Because the threshold to terminate the iteration can vary in different applications, we fixed the iteration number as 10 in the simulation tests. We used Rapidform to create the synthetic target surface and check the deviations [22]. As the second simulation test, we used a human head model. We extracted the skin surface from a patient computed tomography (CT) image and intentionally deformed it using scaling and FFD to create a target surface. The distorted head model was obtained by moving the nodes of FFD in arbitrary directions resulting in deviations of 5.57 ± 3.99 mm (average ± SD) and maximum deviation of 19.96 mm. In the synthetic head model test, the number of points was 6,986 and 6,967 for S and T, respectively. After automatic DSR using RBF-based RPM, we analyzed the deviation between the target T and the registered surface S'. The deviation is computed using the shortest distance between each source point s_i and T. In the tests with real patient data of example applications, we checked not only the visual appearance but also the deviation between T and S', as in the simulation experiments. This retrospective study was approved by the Stanford University School of Medicine Institutional Review Board (No. 16561), and patient information was anonymized.

3. RESULTS

3.1 Performance of RBF-based RPM

Simulation test using a spherical model—Fig. 4 presents the accuracy test results using a synthetic spherical model. While Fig. 4(a) displays S and its deviation; Fig. 4(b) displays S', which matched T perfectly after ten RBF-based RPM iterations. The computing time was 11.6 s on a PC with an Intel i7 3.4 GHz CPU and 12.0 GB RAM. The average

deviation of points between S' and T decreased from 3.81 to 0.18 mm with a decrease ratio of 21.2. The maximum and standard deviations were reduced by ratios of 17.2 and 16.8, respectively, as indicated in Fig. 4(c).

Simulation test using a head model—The simulation test using a human head model and its synthetic target, as indicated in Fig. 5, also yielded promising results. Before local deformation, S and T had maximum deviations of 19.96 mm and average deviations of 5.57 ± 3.99 mm, as indicated in Fig. 5(g). The red circles in Fig. 5(c) indicate parts with significant deviations. The histograms in Figs. 5(e) and 5(f) clearly indicate that the proposed method could deform S to have the same shape as T. After local deformation, the resulting maximum and average deviations were 1.41 and 0.47 ± 0.34 mm, respectively. The maximum and average deviations were reduced by ratios of 14.2 and 11.9, respectively. The average deviation decreased from 5.57 ± 3.99 mm to 0.47 ± 0.34 mm after local deformation. The results presented in Fig. 5 were obtained using ten iterations of RBF-based RPM, and the computing time was 238 s (approximately 4 min) with approximately 7,000 points (n_s = 6,986 and n_t = 6,967).

3.2 Medical applications using RBF-based RPM

In this section, we present three examples of medical applications using RBF-based RPM: patient setup using 3D optical imaging, modification of radiotherapy planning, and patient-specific bone modeling. The detailed background and importance of these medical applications are discussed in Section 4.

Patient setup using 3D optical imaging—A sample application of RBF-based RPM for patient setup in head-and-neck radiotherapy (RT) is illustrated in Fig. 6. As the red circular marking in Fig. 6(a) shows, the target surface extracted from the planning CT is significantly different from the body shape at the treatment obtained from the cone beam CT (CBCT), even after rigid registration using ICP. As indicated in Figs. 6(b) and 6(d), after deformable registration, the source surface obtained at treatment was successfully deformed to match the target surface of the preplanning CT. Fig. 6(c) indicates the source S and its corresponding points t_i. In the red circles of Figs. 6(c) and 6(d), the noticeable discrepancies between S and $\overline{t_i}$ disappeared. The deviation decreased from 1.72 ± 1.88 mm to 0.57 ± 0.66 mm using RBF-based RPM. Then, surgical or RT planning is modified according to the obtained transformation f.

Modification of radiotherapy planning using bone data—Fig. 7 presents the idea of radiotherapy (RT) planning modification using the proposed method, which is based on bone models from the planning and replanning CT. Fig. 7(c) displays the bone models with the tumor volume from the planning CT. Because we already have the RBF transformation function f_{local} (Eqs. (4) and (7)), the interpolation function near the bones is known. We apply f_{local} to modify RT planning by assuming that the soft tissues near the bones will follow the posture change of the bones. Applying RBF interpolation costs only O(n) computation once we have f_{local}. Fig. 7(d) displays the deformed lattice using f_{local}. Fig. 7(e) demonstrates the planning modification for the tumor volume from applying the RBF transformation, which indicates a slightly different shape from the original tumor volume

from the planning CT. In addition to the tumor volume, we can provide an initial prediction for the soft-tissue organs and dose calculation results of RT planning, which can dramatically reduce the preparation time for RT replanning. The tumor volume change after replanning was computed as 0.6 ± 0.51 mm with a maximum deviation of 3.73 mm (Fig. 7(f)).

Patient-specific bone modeling—Fig. 8 illustrates patient-specific femur modeling by using the proposed method. The template model prepared in Fig. 8(a) is deformed to match the patient's femur in Fig. 8(b). As indicated in Fig. 8(b), the patient's femoral model is not refined; hence, it is crude and contains incorrect topology. A 3D patient-specific bone model was successfully created using the proposed method, as illustrated in Fig. 8(d). The deviations before and after the registration are displayed in Figs. 8(e) and 8(f), which are 2.28 ± 1.85 mm and 0.63 ± 0.54 mm, respectively. The runtime for RBF-based RPM was 232 s for surfaces with approximately 4,000 points (n_s = 3,975, n_t = 3,851).

4. Discussion

In Section 3.1, we evaluated the performance of the proposed methods under a simulated environment. Using the simulated models obtained from real patient data, we could measure the theoretical accuracy of the proposed method. Although comparing the exact performances is difficult because of different computing environments, the proposed RBF-based RPM was more than ten times faster than BPM according to the literature of [9]. The average runtime of the BPM algorithm was reported to be 45 min with approximately 4,500 points. Spline-based methods require solving complex surface equations with higher order terms [9, 15], which is inevitably slow. Compared to the spline-based methods, the proposed method is robust and efficient. The proposed method was shown to be robust, which produced stable computational results without any error case from all the tested models. Li et al. [8] also applied RBF for local deformation; however, their deformable registration does not use deformable surface directly; instead, it uses intensity-based volumetric data. In terms of the basis function in RBF, we empirically adopted a multiquadric basis function instead of thin plate spline (TSP). The contribution of the proposed study is a robust and efficient DSR method for medical applications using RBF-based RPM under an annealing fuzzy-based scheme. In our experiments, most of the computing time was consumed in solving the inverse matrix using SVD in the RBF deformation, which can be accelerated if parallel computing is implemented using a graphics processing unit (GPU).

Patient setup using 3D optical imaging

Many approaches to 3D optical imaging for patient setup have been proposed recently in surgery [23, 24] and RT [25-28]. 3D optical imaging for patient setup is advantageous because it is radiation free and can even monitor patient movement by capturing data in near real time [29]. Moreover, 3D scanning for patient setup provides greater patient comfort compared to conventional invasive methods such as stereotactic frames in brain surgery. Patient positioning is an important step in improving surgery and RT accuracy. To improve surgery or RT outcome, the preoperative or RT planning data must accurately match the intraoperative data. Thus, accurate registration is a key technology for patient setup using 3D

optical imaging and RBF-based RPM can improve the registration result. The proposed method can be utilized to overcome the problem of surface shape change and noise/defects from 3D optical imaging for accurate patient setup.

Modification of radiotherapy planning using bone data

Multi-fractional RT, which requires multiple treatments, is a common protocol in RT. RT replanning occurs during long-term tumor treatment for several reasons: tumor size or shape change, patient weight loss, and patient posture change. If the clinician decides to replan, RT planning is performed anew based on the replanning CT. Typically, RT planning requires substantial time and effort for segmentation and dose calculation. Al-Mayah et al. [30] investigated a biomechanical-based image registration for head-and-neck RT and found that aligning the vertebrae and mandible improves neighboring soft tissue targeting, including the tumor. Veiga et al. [31] suggested adaptive radiotherapy (ART) using deformable registration with B-spline FFD, a volumetric registration method. Similarly, we can use RBF-based RPM for RT planning modification. Although each bone is a rigid body, the set of head-and-neck bones, including mandible and cervical vertebrae, can be regarded as a deformable model. The results in Section 3.2 indicate that the application of RBF-based RPM is feasible in adaptive treatment for head-and-neck RT planning. Further study is required to measure the target registration error (TRE). Once deformable registration is performed, the target (such as tumor) location can be computed. For example, the predicted result of the deformed tumor by the RBF-based RPM can be compared to the real tumor location from the intraoperative CBCT. In this case, the predicted tumor is computed by RBF-RPM using preoperative CT (source) and intraoperative CBCT (target), and the result is compared with the model directly obtained from the real intraoperative CBCT.

Patient-specific bone modeling

3D patient-specific modeling is gaining increasing popularity in many medical fields such as tissue engineering using 3D printing [32], finite element method (FEM) analysis [33], and diagnosis/treatment planning and surgical simulation [34]. Effective patient-specific modeling can be achieved using the proposed method with a template model. Once we have a prepared template with perfect topology and geometry for representative cases, RBF-based RPM can create a patient-specific model by deforming the template model. From the coarse data of an individual’s CT or other types of radiographic images, the template model as S is deformed to the coarse patient data as T. A similar approach in segmentation of patient specific 3D organ modeling can be found in [35].

5. Conclusion

We proposed a robust and efficient RBF-based RPM method for DSR suitable for various medical applications. The proposed method can eliminate the deviation of two input surfaces and is significantly faster than the previous method of B-spline-based RPM. We demonstrated the effectiveness of RBF-based RPM by suggesting typical applications: patient setup using 3D optical imaging, modification of radiotherapy planning using bone data, and patient-specific modeling. We plan to accelerate RBF deformation by implementing GPU-based computing along with further investigation on the clinical study of

the sample applications presented in this paper, including an analysis on target registration error and clinical feasibility.

Supplementary Material

Refer to Web version on PubMed Central for supplementary material.

Acknowledgement

This research was supported in part by the KIST institutional program (2E26210, 2E26276), and the NIH (R01EB016777).

References

[1]. Crum WR, Hartkens T, Hill DLG. Non-rigid image registration: theory and practice. Br J Radiol. 2014; 77:140–53.

[2]. Carter TJ, Sermesant M, Cash DM, Barratt DC, Tanner C, Hawkes DJ. Application of soft tissue modelling to image-guided surgery. Med Eng Phys. 2005; 27:897–909.

[3]. Maes F, Collignon A, Vandermeulen D, Marchal G, Suetens P. Multimodality Image Registration by Maximization of Mutual Information. IEEE Trans Med Imag. 1997; 16(2):187–98.

[4]. Rueckert D, Sonoda LI, Hayes C, Hill DLG, Leach MO, Hawkes DJ. Nonrigid registration using free-form deformations: application to breast MR images. IEEE Trans Med Imag. 1999; 18(8): 712–21.

[5]. Modata M, Ridgwaya GR, Taylora ZA, Lehmannb M, Barnesb J, Hawkesa DJ, Foxb NC, Ourselina S. Fast free-form deformation using graphics processing units. Comput Method Progr Biomed. 2010; 98(3):278–84.

[6]. Nithiananthan S, Brock KK, Daly MJ, Chan H, Irish JC, Siewerdsen JH. Demons deformable registration for CBCT-guided procedures in the head and neck: Convergence and accuracy. Med Phys. 2009; 36(10):4755–64. [PubMed: 19928106]

[7]. Gu X, Pan H, Liang Y, Castillo R, Yang D, Choi D, et al. Implementation and evaluation of various demons deformable image registration algorithms on a GPU. Phys Med Biol. 2010; 55(1):207–19. [PubMed: 20009197]

[8]. Li X, Yankeelov TE, Peterson TE, Gore JC, Dawant BM. Automatic nonrigid registration of whole body CT mice images. Med Phys. 2008; 35(4):1507–20. [PubMed: 18491546]

[9]. Wang H, Fei B. Nonrigid point registration for 2D curves and 3D surfaces and its various applications. Phys Med Biol. 2013; 58:4315–30. [PubMed: 23732538]

[10]. Carr, JC.; Beatson, RK.; Cherrie, JB.; Mitchell, TJ.; Fright, WR.; McCallum, BC.; Evans, TR. Reconstruction and representation of 3D objects with radial basis functions; Comput Gr (SIGGRAPH ’01 Conf. Proc.); 2001. p. 67-76.

[11]. Li, H.; Adams, B.; Guibas, LJ.; Pauly, M. Robust single-view geometry and motion reconstruction; ACM Trans Gr, (SIGGRAPH Asia ’09 Conf. Proc.); 2009.

[12]. Bonarrigo F, Signoroni A, Botsch M. Deformable registration using patch-wise shape matching. Gr Model. 2014; 76(5):554–65.

[13]. Myronenko A, Song X. Point set registration: coherent point drift. IEEE Trans Pattern Anal Mach Intell. 2010; 32(12):2262–75. [PubMed: 20975122]

[14]. Jian B, Vemuri BC. Robust point set registration using gaussian mixture models. IEEE Trans Pattern Anal Mach Intell. 2011; 33(8):1633–45. [PubMed: 21173443]

[15]. Gold S, Rangarajan A, Lu CP, Pappu S, Mjolsness E. New algorithms for 2-D and 3-D point matching: pose estimation and correspondence. Pattern Recognit. 1998; 31:1019–31.

[16]. Chui H, Rangarajan A. A new point matching algorithm for non-rigid registration. Comput Vis Imag Underst. 2003; 89:114–41.

[17]. Xie Z, Farin GE. Image registration using hierarchical B-splines. IEEE Trans Visual Comput Gr. 2004; 10(1):85–94.

[18]. Zhang Z. Iterative point matching for registration of free-form curves and surfaces. Int J Comput Vis. 1994; 13(2):119–52.

[19]. Chen Y. Object modeling by registration of multiple range images. IEEE Int Conf Rob and Autom. 1991; 3:2724–2729.

[20]. Kim Y, Lee K, Kim W. 3D virtual simulator for breast plastic surgery. Comput Anim Virtual World. 2008; 19:515–26.

[21]. Press WH, Teukolsky SA, Vetterling WT, Flannery BP. Numerical Recipes 3rd Edition: The Art of Scientific Computing. Cambridge University Press. 2007:59–70.

[22]. RapidForm, 3D Systems Co.. http://rapidform.com

[23]. Shamir RR, Freiman M, Skowicz L, Spektor S, Shoshan Y. Surface-based facial scan registration in neuronavigation procedures: a clinical study. J Neurosurg. 2009; 3(6):1201–6. [PubMed: 19392604]

[24]. Frisardi G, Chessa G, Barone S, Paoli A, Razionale A, Frisardi F. Integration of 3D anatomical data obtained by CT imaging and 3D optical scanning for computer aided implant surgery. BMC Med Imag. 2011; 11(5)

[25]. Nath SK, Lawson D, Wang JZ, Simpson DR, Newman CB, Alksne JF, Mundt AJ, Murphy KT. Optically guided frameless linac-based radiosurgery for brain metastases: clinical experience. J Neurooncol. 2010; 97(1):67–72. [PubMed: 19701719]

[26]. Pan H, Cervino LI, Pawlicki T, Jiang SB, Alksne J, Detorie N, et al. Frameless, Real-Time, Surface Imaging-Guided Radiosurgery: Clinical Outcomes for Brain Metastases. Neurosurg. 2012; 71(4):844–51.

[27]. Shah AP, Dvorak T, Curry MS, Buchholz DJ, Meeks SL. Clinical evaluation of interfractional variations for whole breast radiotherapy using 3-dimensional surface imaging. Pract Radiat Oncol. 2012; 3(1):16–25. [PubMed: 24674259]

[28]. AlignRT, VisionRT Inc.. http://www.visionrt.com/

[29]. Sentinel, C-RAD Inc.. http://www.c-rad.com/

[30]. Al-Mayah A, Moseley J, Hunter S, Velee M, Chau L, Breen S, Brock K. Biomechnical-based image registration for head and neck radiation treatment. Phys Med Biol. 2010; 55:6491–500. [PubMed: 20959687]

[31]. Veiga C, McClelland J, Moinuddin S, Lourenço A, Ricketts K, Annkah J, et al. Toward adaptive radiotherapy for head and neck patients: Feasibility study on using CT-to-CBCT deformable registration for "dose of the day" calculations. Med Phys. 2014; 41(3):031703. [PubMed: 24593707]

[32]. Hutmacher DW, Sittinger M, Risbud MV. Scaffold-based tissue engineering: rationale for computer-aided design and solid free-form fabrication systems. Trend Biotech. 2004; 22(7):354–62.

[33]. Poelert S, Valstar E, Weinans H, Zadpoor AA. Patient-specific finite element modeling of bones. Proc Inst Mech Eng H. 2013; 227(4):464–78. [PubMed: 23637222]

[34]. Thalmann NM, Choi HF, Thalmann D. Towards Effective Diagnosis and Prediction via 3D Patient Model: A Complete Research Plan. 3D Multiscale Physiol Hum. 2014:3–22.

[35]. Berendsen FF, Heide UA, Langerak TR, Kotte ANTJ, Pluim JPW. Segmentation of Cervical Images by Inter-subject Registration with a Statistical Organ Model. Abdom Imag Comput Clin Appl, LNCS. 2012; 7029:240–7.

Prepare the source and target surface point sets
Compute the global transformation $\boldsymbol{f}_{global}$ by iterative closest points
Initialize the temperature parameter κ_0=0.5
Repeat iterations until the convergence below a threshold difference
  Update the correspondence matrix $\boldsymbol{M}$
  Compute the local deformation $\boldsymbol{f}_{local}$ by RBF and the correspondence
  Decrease $\kappa_{n+1}=0.9\cdot\kappa_n$

Figure 1.
Pseudocode of RBF-based robust point-matching algorithm.

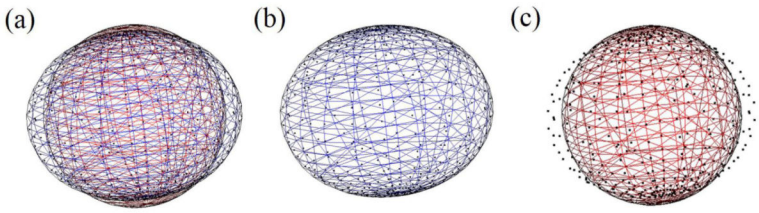

Figure 2.

Automatic correspondence finding. (a) The sphere-shaped source surface in red and the distorted target surface in blue, (b) the target surface and the corresponding points (note that the black corresponding points are located differently from the vertices of target surface), (c) the source surface and the corresponding points.

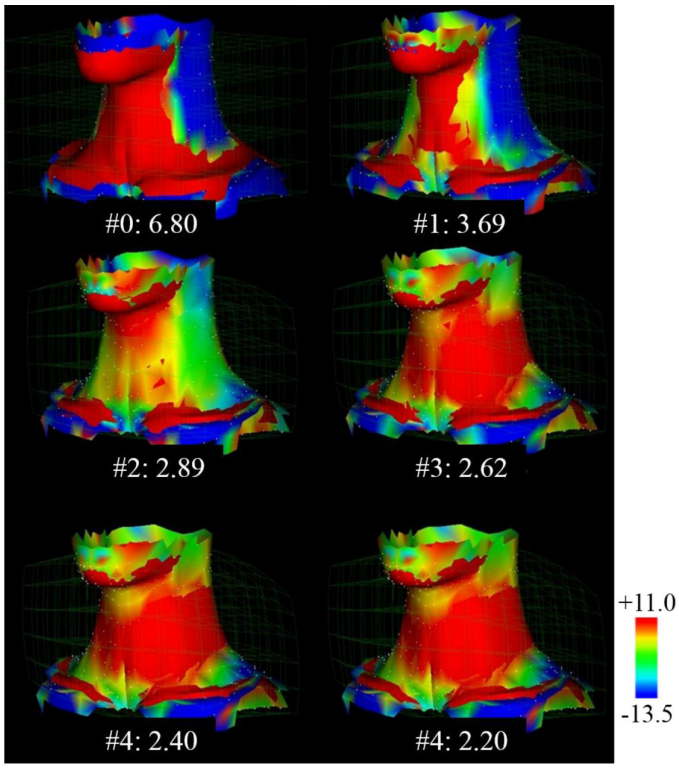

Figure 3.
Deformable registration results according to the number of iterations. The average deviation decreases through iteration as indicated underneath each figure. The source surface S is red, and deviations were visualized by color-map in target surface T (Unit: mm).

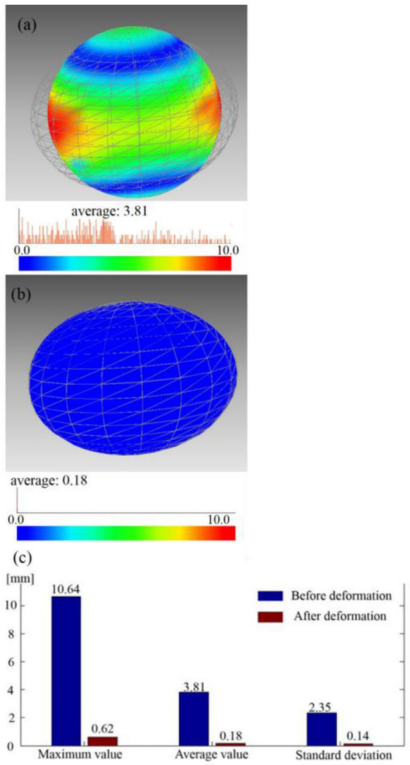

Figure 4.

Accuracy test results using a spherical model and its synthetic target. The deviation between the source (color-mapped) and target (wire-framed) (a) before and (b) after RBF-based RPM. (c) Maximum, average, and standard deviations between before and after deformations. (Unit: mm)

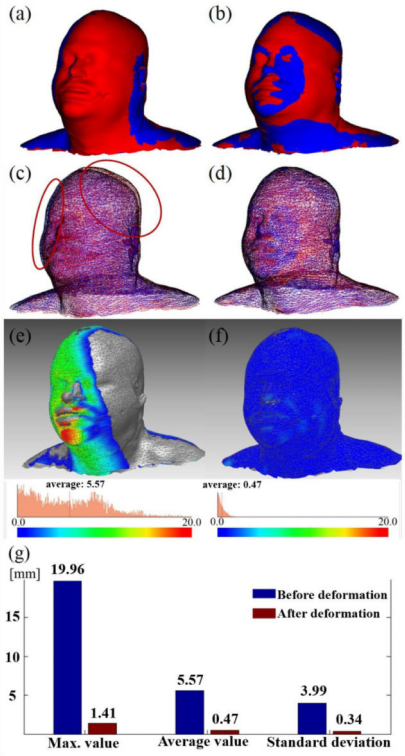

Figure 5.

Accuracy test results using a human head model and its synthetic target. The left ((a), (c), (e)) and right ((b), (d), (f)) columns show results before and after registration, respectively. The models in (a) and (b) are in shade mode; those in (c) and (d) are in the wire-frame mode. In (a)-(d), S and T are in red and blue, respectively. The red-circles in (c) indicate the parts with significant deviations. (e) and (f) display the deviation with a color-mapped model. (g) Maximum, average, and standard deviations are compared between before and after deformations. (Unit: mm)

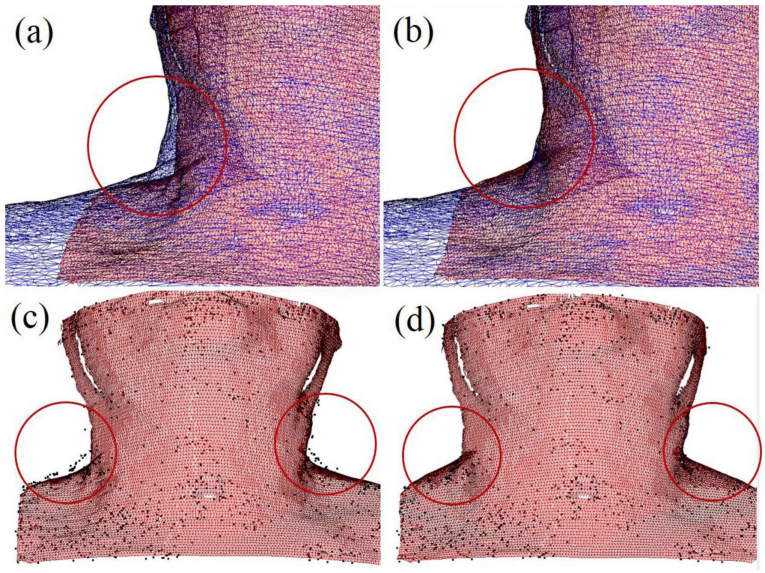

Figure 6.

Example of patient setup using 3D optical scanning. (a) and (c): before deformable registration after rigid registration using ICP; (b) and (d): after deformable registration using RBF-based RPM (blue surface: body surface extracted from planning CT, red surface: body surface extracted from CBCT, assuming the 3D optical scanning data). (a) and (b) display the source and target surfaces; (c) and (d) display the source (intraoperative data) and its corresponding points (planning CT).

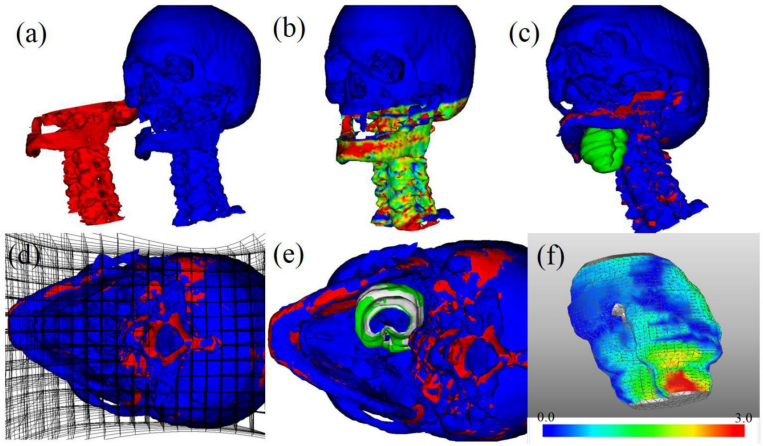

Figure 7.

Radiotherapy planning modification example. (a) Bone models from the planning CT (blue) and replanning CT (red), (b) after registration, (c) bone model with planning CT tumor volume (green), (d) lattice deformation using RBF deformation, (e) modified tumor volume using RBF-based RPM, and (f) deviation of tumor volume between before and after planning modification (Unit: mm).

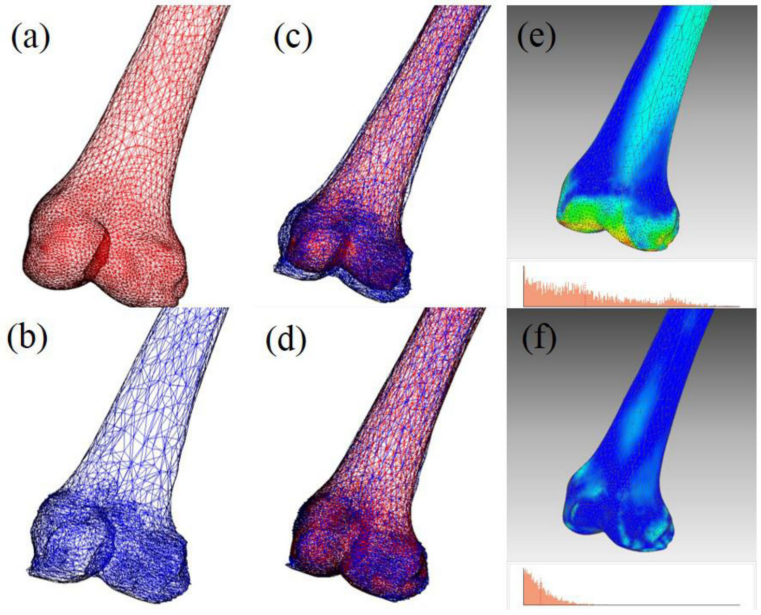

Figure 8.

Patient-specific femur modeling example. (a) template femoral model (3,975 points and 7,908 triangles), (b) specific patient's bone model (3,851 points and 7,682 triangles), (c) after rigid registration by ICP, (d) after deformable registration using RBF-based RPM, (e) deviation before deformable registration, and (f) deviation after registration.